JACS
JOURNAL OF THE AMERICAN CHEMICAL SOCIETY
pubs.acs.org/JACS
Article

Growing and Shaping Metal–Organic Framework Single Crystals at the Millimeter Scale

Alessandro Sorrenti, Lewis Jones, Semih Sevim, Xiaobao Cao, Andrew J. deMello, Carlos Martí-Gastaldo,* and Josep Puigmartí-Luis*

Cite This: J. Am. Chem. Soc. 2020, 142, 9372–9381

ABSTRACT: Controlling and understanding the mechanisms that harness crystallization processes is of utmost importance in contemporary materials science and, in particular, in the realm of reticular solids where it still remains a great challenge. In this work, we show that environments mimicking microgravity conditions can harness the size and shape of functional biogenic crystals such as peptide-based metal–organic frameworks (MOFs). In particular, we demonstrate formation of the largest single crystals with controlled nonequilibrium shapes of peptide-based MOFs reported to date (e.g., those featuring curved crystal habits), as opposed to the typical polyhedral microcrystals obtained under bulk crystallization conditions. Such unique nonequilibrium morphologies arise from the interplay between the diffusion-controlled supply of precursors in simulated microgravity environments and the physical constraints imposed during crystal growth. In fact, our method mimics two main strategies of morphogenesis in biomineralization, i.e., spatial and morphological control, both being largely unexplored in the field of self-assembled functional materials. The presented results may open new opportunities to study and understand fundamental questions of relevance to materials science, such as how the size and shape of artificial crystals can influence their properties and functions while providing a strategy to tailor the size and shape of peptide-based MOF single crystals to specific applications.

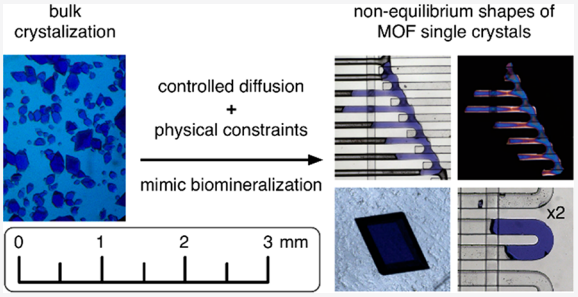

INTRODUCTION

Crystallization is a dynamic process that has long been used in the evolution of living organisms but is still barely understood and poorly controlled in modern science. In nature, biomineralization processes are used to produce unique crystal structures with an exquisite control over size, shape, and composition.[1−3] This results in remarkably complex morphologies and functions with no analogues in the artificial counterpart.[1,4] Biominerals, for example, can change their catalytic activity, transport behavior, and even separation efficiencies by controlling the size and shape of the final product.[1] In this vein, biomineralization has long served as a source of inspiration to the research community.[1−3,5,6] For example, polymeric soft templates or selective growth inhibitors, which mimic biomineralization strategies, have been extensively used to control the habit of inorganic crystals such as calcite.[2,5,7−9] In the field of metal–organic frameworks (MOF) much effort has been put in the morphological control of crystals at the nano- and microscale during their bulk synthesis as well as into their processing at the mesoscale (e.g., into polycrystalline films, patterns, and composites).[10−12] Strategies such as modulation of reaction parameters and preparation protocols, use of additives (e.g., modulators, blocking agents), or reaction at the interface of biphasic systems have been explored.[10,11] Recently, formation of macro–microporous MOF single crystals of micrometer size has been achieved using a templating approach together with a double-solvent-induced nucleation method.[13,14] However, precise control over both the size and the shape of macroscopic single crystals of self-assembled functional materials, such as MOFs, is still a great challenge, with the mechanisms and processes underpinning crystal growth remaining largely unresolved. Unlike crystals, macromolecules such as proteins are able to change conformation, structure, and/or function due to low-energy torsions in their structure.[15,16] These changes are often accomplished following multiple pathways and in response to changes in their surrounding environment and are vital to their biological function.[17] Recently, a new family of functional porous crystalline structures capable of torsion and conformational changes reminiscent of proteins has emerged in the realm of reticular solids. Peptide-based MOFs are assembled by the interlinking of metal ions to oligopeptide linkers[18−21] and have

Received: February 18, 2020
Published: April 18, 2020

https://dx.doi.org/10.1021/jacs.0c01935
J. Am. Chem. Soc. 2020, 142, 9372–9381

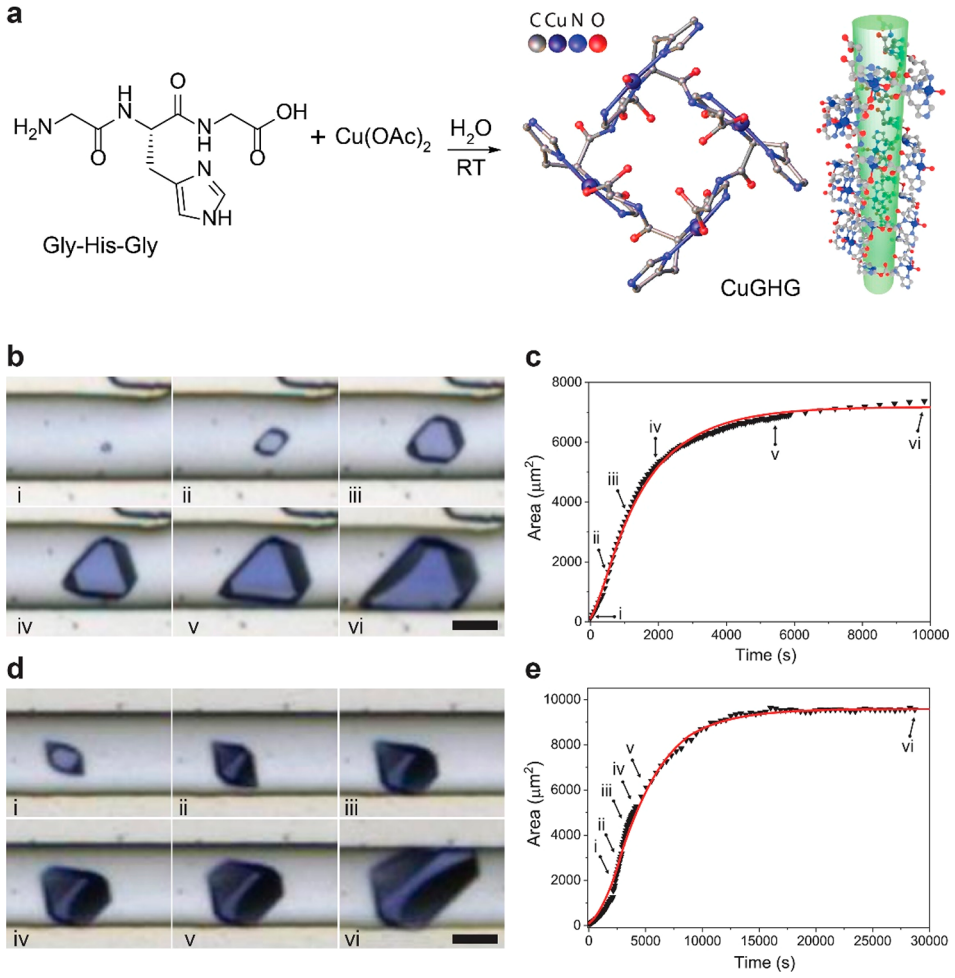

Figure 1. Growth of CuGH crystals in closed microchambers (confined growth). (a) Chiral tripeptide GHG complexes Cu^{2+} to form the 3D framework CuGHG. (b and d) Images taken at different times during growth of two exemplary CuGHG crystals, Crystal 1 and Crystal 2, respectively. Roman numerals (i–vi) correspond to selected time points indicated in the corresponding panels c and e. Scale bars correspond to 50 μm. (c and e) Area versus time plots representing the growth kinetics of Crystal 1 and Crystal 2, respectively. Symbols are experimental data, with lines being best fits to the experimental data from the physical model based on reaction–diffusion theory.

gained much attention due to the rearrangement of their framework, which is enabled by the rich conformational landscape accessible to the peptide linkers.[19] This conformational mobility can lead to new advanced functions not accessible to their rigid counterparts.[20,22] In a similar manner to classical MOFs, the size, shape, and chemistry of the pores can be precisely controlled in these materials at the atomic level, but the final size and morphology of their crystals are determined by crystallographic parameters and surface growth kinetics.[11] As a result, typical bulk crystallization results in isolation of polyhedral-faceted microcrystals that are often difficult to process, for example, as stationary phases for chiral separation. The latter is an application in which this family of solids has great potential.[23,24] Accordingly, it is evident that routes to obtaining macroscopic single crystals of adaptable porous frameworks with controllable size and shape,[25] as opposed to polycrystalline monoliths, are of high current interest.[11,12]

Crystallization experiments conducted in space have previously shown that microgravity conditions can lead to larger protein crystals with superior diffraction properties.[26] Microgravity environments are characterized by low Grashof numbers,[27] conditions that can be also achieved using microfluidic devices, where viscous forces dominate buoyancy forces.[28,29] Herein, we demonstrate that such conditions can be used to mimic biomineralization processes and to accomplish nonequilibrium shapes during growth of CuGHG, a peptide-based MOF formed by coordination of the tripeptide glycine-L-histidine-glycine (GHG) to Cu^{2+} to assemble a 3D framework (Figure 1a).[22,24]

RESULTS AND DISCUSSION

One of the key mechanisms of morphogenesis in biomineralization is compartmentalization, i.e., formation of enclosed spaces that both allow the regulation of supersaturation levels through controlled reactant diffusion and provide a physical barrier that can directly cast the crystal shape.[1,5] By confining CuGHG crystal growth within spaces that simulate microgravity conditions, namely, advection-free microfluidic environments,[30,31] we have been able to mimic such a regulation strategy, which is still essentially unexplored in materials chemistry, particularly in the field of self-assembled functional materials and reticular solids. Initially, we generated confined submicroliter spaces within a polydimethylsiloxane (PDMS)-based double-layer microfluidic device (Type I device), which comprises a branched fluidic circuit (fluid layer) and

https://dx.doi.org/10.1021/jacs.0c01935
J. Am. Chem. Soc. 2020, 142, 9372–9381

pneumatic valves (control layer)[32] (Supplementary Figure 1). Type I devices were fabricated via multilayer soft lithography (Experimental Section and Supplementary Note 1).[32] In a typical experiment, a supersaturated solution containing equimolar amounts of Cu^{2+} and peptide is injected into the fluid layer, followed by actuation of the pneumatic valves, which enable isolation of elongated microchambers with a width of 100 μm and volumes that range between 0.6 and 6.4 nL. After a variable lag phase, usually between a few minutes and 1 h, deep blue polyhedral CuGHG crystals start to appear and grow from the metastable precursor solution, as can be directly observed by optical microscopy (Supplementary Video 1). Hereafter, we refer to the crystallization process within such microchambers as confined growth. Typically, only 1−2 crystallization events occur in a single microchamber, which allowed us to assess the growth kinetics at the level of the single crystal via time-lapse optical imaging. The limited number of crystallization events can be ascribed to the rapid depletion of precursors resulting from growth of the first crystal(s) in the nanoliter microchambers, which decreases the solute concentration and prevents further nucleation.[33] We observed that the onset of crystallization occurs stochastically in different microchambers with no obvious correlation between the lag time and the microchamber volume (Supplementary Figure 3). Accordingly, we did not further investigate the nucleation kinetics but rather focus on assessing crystal growth kinetics,[34] starting from when a crystal is initially detected under the microscope.

Figure 1b and 1d shows a series of snapshots taken at different times during the growth of two exemplary CuGHG crystals: Crystal 1 and Crystal 2. Complete movies of the nucleation and growth of various crystals are shown in Supplementary Video 1. According to the literature, reaction of Cu^{2+} with GHG can result in formation of different crystallographic phases of increasing symmetry, ranging from monoclinic to orthorhombic and tetragonal structures (CSD reference codes GLHGCU, GHGCUS, and sntA00023C1) due to slight differences in the synthetic conditions.[22,35,36] We targeted the synthesis of the tetragonal phase that corresponds to the 3D porous peptide MOF. To confirm phase purity, we analyzed 15 crystals grown in 5 Type I devices with x-Ray diffraction. Those crystals were recovered by split opening the PDMS layers in absolute ethanol. All crystals were consistently indexed with a tetragonal $P4_12_12$ space group (a = 14.08(6) Å, c = 27.02(7) Å) in agreement with formation of CuGHG crystals inside the microchambers (Supplementary Figure 4). Time-lapse recordings of the crystal growth were subject to image segmentation using a machine-learning technique[37] followed by thresholding and particle analysis to determine crystal area and perimeter variations (Experimental Section, Supplementary Video 2, and Supplementary Figure 5). Representative area vs time plots show a pseudo-sigmoidal profile (Figure 1c and 1e), where the growth rate initially increases due to an increase in the crystal perimeter in contact with solution, reaches a maximum and then slows down until the curve plateaus due to precursor depletion in diffusion-controlled conditions. To achieve additional insight into the crystal growth dynamics within our advection-free microchambers, we established a physical model within the framework of reaction−diffusion (RD) theory based on the "two resistances in series approach"[34,38] (Experimental Section and Supplementary Note 2). The model (Experimental Section eq 6) was used to fit the experimental data by a global minimization procedure, resulting in a good fit (red curves in Figure 1c and 1e). From the model, the contribution of the two coupled processes involved in crystal growth, i.e., diffusion of the solute from the bulk solution to the crystal interface and its integration into the growing crystal,[34] could be evaluated and the values of the coefficients of mass transfer by diffusion (k_d) and reaction (k_r) estimated with a good approximation (Supplementary Note 3, Table 2, and Figure 7). Results reveal that the overall growth rate is strongly dependent on the diffusion step, with k_d values ranging between the same order of magnitude to 10 times lower than those of k_r for the analyzed crystals (e.g., k_d/k_r = 1.4(7) for Crystal 2 and 0.1(1) for Crystal 1). Note that when k_d values are comparable to or much smaller than those of k_r, diffusion of the precursors strongly affects the growth kinetics influencing the overall experimental growth rate k_G.(Experimental Section eq 7); on the contrary, a crystallization process is purely reaction limited if $k_r \ll k_d$.[34,38] These results arise from crystal growth occurring in a confined advection-free environment, where mass transfer only occurs via pure molecular diffusion.[30,33] In fact, under conditions that mimic microgravity, crystal growth induces development of a depletion zone that is not disrupted by natural convection.[26,33] To demonstrate the validity of our model, we measured the diffusion coefficient for the molecular chelate complex CuGHG(aq)[39] in water by diffusion ordered spectroscopy (DOSY-NMR). The obtained values are in good agreement with the magnitude of diffusivity estimated from k_d (Supplementary Table 2 and Note 4). In addition, because of the finite dimensions of the microchambers used for the confined growth experiments, the diffusive front starting from the crystal and propagating outward reaches the ends of channels in less than 90 min after the onset of crystallization, as estimated by the value of the diffusion coefficient (Supplementary Note 4).[38,40] Accordingly, the confined growth process, which spans several hours, is heavily controlled by precursor depletion in the absence of replenishment. In contrast, we found that the values of k_r are about 1 order of magnitude different for the two crystals investigated (k_r' = 1.49 and 0.21 μm s^{-1} for Crystal 1 and Crystal 2, respectively, see Supplementary Note 3), resulting in faster growth for Crystal 1 (Figure 1c, Supplementary Table 2, and Figure 7). We ascribe this difference to the different orientation of the growing crystals inside the microfluidic channels resulting in a diverse exposure of their fast- and slow-growing faces to either the precursor solution or the channels walls. This difference suggests the possibility of achieving control over the generation of nonequilibrium shapes for CuGHG crystals within confined spaces (vide infra). Furthermore, studying CuGHG crystallization inside Type I devices (which comprises microchambers with known volume) and knowing the concentration of the precursor solution allowed us to introduce mass-balance considerations in the kinetic model and thus to extract additional quantitative information from the fitting (Experimental Section). We defined a fitting parameter σ_{eff}, which is related to the actual fraction of the starting materials (number of moles) that is incorporated in the crystal at the plateau, where $1 - \sigma_{eff}$ is the yield of crystallization. From σ_{eff}, we could calculate the average concentration of the depleted growth media, C^*, which surrounds fully grown crystals (i.e., at the plateau of the growth kinetic profiles) (Supplementary Table 2). Surprisingly, we found that C^* can drop significantly below the solubility value of CuGHG(aq) in water, i.e., 110 ± 10 mM

https://dx.doi.org/10.1021/jacs.0c01935
J. Am. Chem. Soc. 2020, 142, 9372−9381

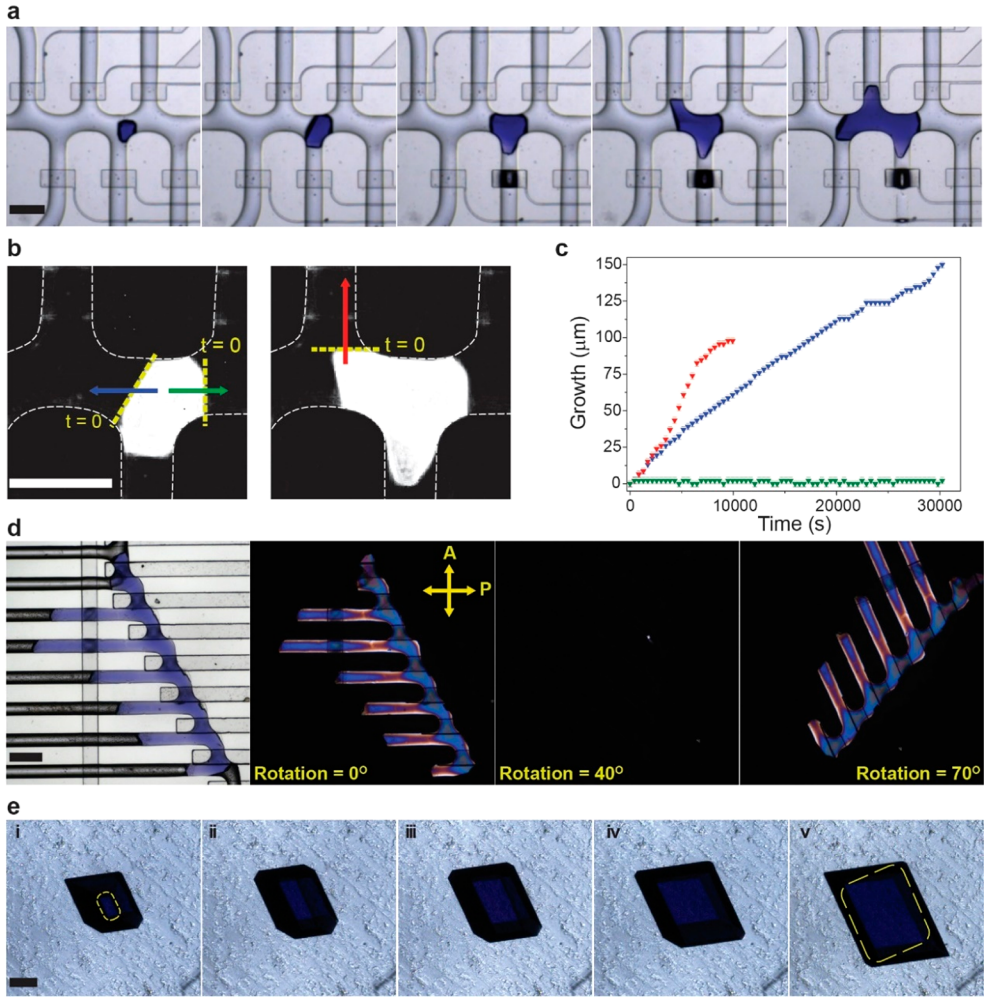

Figure 2. Shaping CuGHG single crystals by confined growth. (a) Bright-field images showing the confined growth of a branched CuGHG single crystal within a Type II microfluidic device (Supplementary Video 4 shows the entire growth process). Scale bar corresponds to 100 μm. (b) Binary probability maps corresponding to two snapshots along the growth of the crystal shown in a. Arrows (blue, green, and red) indicate the three directions along which linear growth was measured, while dashed lines indicate the corresponding starting positions from which the linear growth was measured. (c) Linear growth along the directions blue, green, red indicted in b, i.e., displacement of the crystal interface as a function of time from the initial positions indicated in b. (d) Comb-shaped CuGHG single crystal grown in a Type I device. From left to right: bright field and three cross polarized images showing different relative orientations of the crystal with respect to the crossed polars (P = polarizer, A = analyzer). Crystal is birefringent and extinguishes simultaneously at 40° (and 130°, 220°, 310°), exhibiting single-crystal behavior. (e) Bright field images along the growth of a CuGHG single crystal with a 2D flat morphology within a Type III device. Yellow dashed lines surround the flat surface of the crystal that contacts the ceiling of the chamber and indicates that growth is restrained along the perpendicular Z direction (height of the chamber = 200 μm). Scale bars in d and e correspond to 200 μm.

at 24 °C, which was determined by bulk crystallization experiments (Experimental Section and Supplementary Note 4). For example, C^* = 78.6 mM for Crystal 2 (Supplementary Table 2). This is in agreement with the experimental observation that the flow of the depleted growth media through formed crystals, e.g., induced by the opening of a pneumatic valve, often results in their prompt dissolution. This result supports the possibility of generating nonequilibrium crystal forms of CuGHG in contact with an undersaturated solution of precursors by confined growth. We argue that this effect is due to the sequestration of crystal surfaces by the microfluidic channel walls as crystals grow to occupy the entire channel cross section (vide infra). Accordingly, a large portion of the surface is excluded from contact with the monomer solution and thus removed from crystallization equilibrium. This sequestration shifts the equilibrium toward the crystalline phase and results in maximal monomer depletion.

A closer look at the growth process reveals that at the beginning, when the crystal size is smaller than the channel dimensions, most crystals feature a similar polyhedron habit in which crystalline faces are clearly detectable. This morphology can be regarded as the equilibrium morphology of CuGHG crystals. However, as growth proceeds, sudden changes of the growth rate along different directions are observed, as determined by the formed local chemical gradients and geometric constraints. As a result, CuGHG crystals lose their initial polyhedron habit, take the shape of the microchamber in which they are growing, and entirely fill the chamber cross-section (Supplementary Video 3 and Supplementary Figure 10). This is obvious from scanning electron microscopy (SEM) images that show crystals with a smooth curved surface and the shape of a horizontal cylindrical segment, where the crystalline faces are no longer detectable (Supplementary Figure 11). Guided by these observations, we next explored the

https://dx.doi.org/10.1021/jacs.0c01935
J. Am. Chem. Soc. 2020, 142, 9372−9381

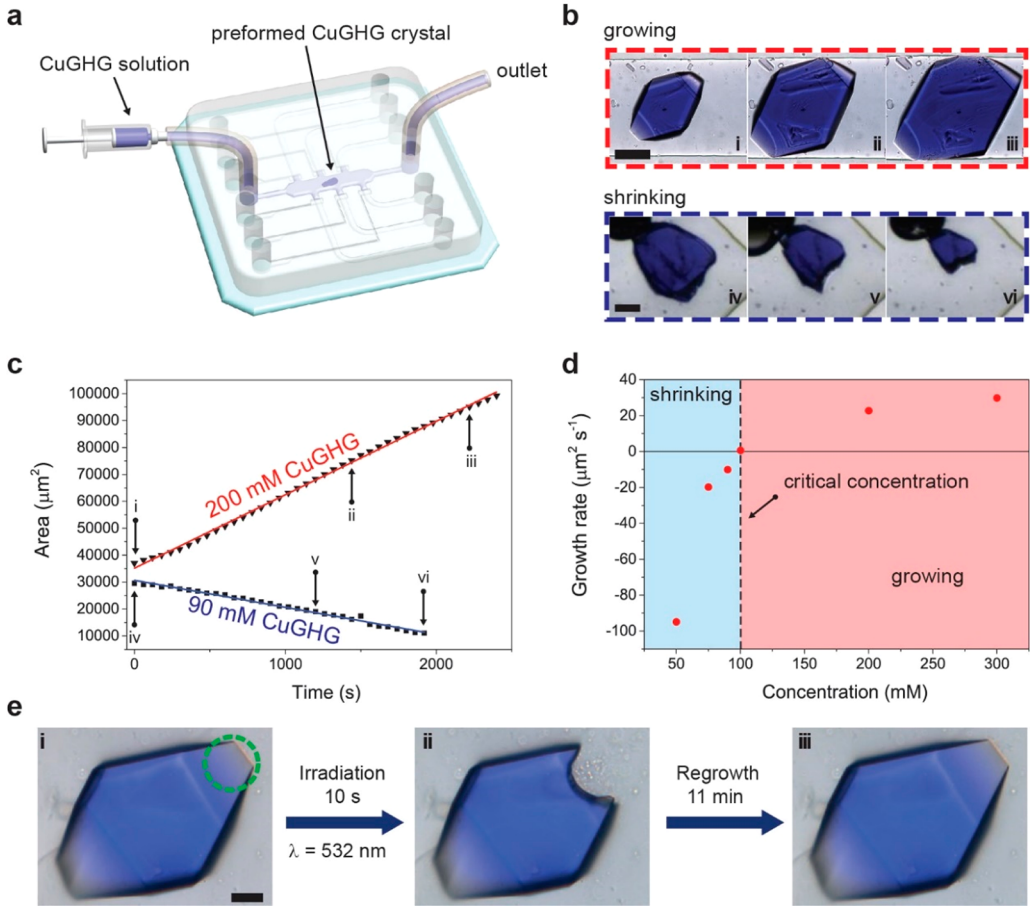

Figure 3. Growth and shrinkage of CuGHG crystals under continuous feeding and crystal regrowth after laser-induced damage. (a) Schematic of the Type II device used to expose preformed CuGHG crystals, previously obtained by confined growth, to a continuous flow (1 μL min^{-1}) of an equimolar solution of Cu^{2+} and GHG. Either further growth or shrinking of the crystals was observed depending on the concentration of the feeding solution. (b) Snapshots showing the growth or shrinkage observed when flowing a 200 or 90 mM precursor solution (scale bars correspond to 100 and 50 μm, respectively). (c) Plots of the crystal area as a function of time showing that under continuous feeding both growth (black triangles) and shrinkage (black squares) follow linear kinetics. Continuous lines represent the linear fit from which the respective rates were obtained. (d) Growing/shrinkage rates as a function of the concentration of the feeding solution. Critical concentration of about 100 mM separates the two domains. (e) Light micrographs showing laser-induced damage and complete regrowth of a CuGHG single crystal within a microfluidic space. Specifically, a fully grown CuGHG crystal (i) was irradiated for 10 s with a 532 nm laser (focused on the outlined region) resulting in extensive damage (ii). After turning off the laser, fast (11 min) and complete regrowth of the irradiated part was observed with memory of the original shape (iii). Images correspond to the fifth cycle of blasting/regrowth. See Supplementary Video 8. Scale bar in e corresponds to 10 μm.

possibility of preparing CuGHG crystals with more complex nonequilibrium morphologies by confining their growth in other microfluidic devices that offer more possibilities to create concentration gradients and studying their effect on crystal growth. On the basis of our findings using the kinetic model and knowing that the crystal growth kinetics strongly depend on the diffusion of precursors, we designed Type II devices (Supplementary Figure 2). These devices consist of a branched fluid layer with nine inlets, where the effect of concentration gradients and geometrical constraints can be assessed during CuGHG crystal growth. Figure 2a shows snapshots of confined growth of a single CuGHG crystal within a Type II device, resulting in an unprecedented branched morphology for a monolith MOF crystal (a full recording is provided in Supplementary Video 4).

Anisotropic growth is clearly evident in the corresponding time-lapse recording with markedly different growth rates measured along different geometric directions. For example, rates of 0 and 18 μm h^{-1} were observed, respectively, for growth along the right and left directions of the main channel (green and blue arrows in Figure 2b), as measured from the respective growth vs time profiles (Figure 2c). In addition, a sudden acceleration of growth is observed along the vertical direction (red arrow in Figure 2b) as soon as the growing interface is exposed to the solution of the vertical branch (red plot in Figure 2c and Supplementary Video 4). Remarkably, morphogenesis of the CuGHG crystal in Figure 2a arises from the interplay of three main factors governing anisotropic growth, i.e., (i) local concentration gradients influencing the availability of precursors, (ii) physical constraints imposed by the channel walls, and (iii) orientation of the fast and slow faces of the growing crystal with respect to the microfluidic channel. The latter determines whether those crystal faces are exposed to or hidden from the precursor solution. We point out that these mechanisms can only operate because of the unique physical conditions present in our microfluidic environments.[31] Put simply, geometrical confinement, absence of advection, and sequestration of crystal surfaces by PDMS walls ultimately leads to CuGHG crystal shapes not achievable by conventional crystallization from solution.[22,24]

https://dx.doi.org/10.1021/jacs.0c01935
J. Am. Chem. Soc. 2020, 142, 9372−9381

To clearly demonstrate these assumptions based on the experimental observations acquired in Type II devices, we extended the shape-controlled growth of CuGHG crystals to Type I devices (Supplementary Figure 1). In these experiments, the lateral pneumatic valves were not actuated, resulting in the formation of a comb-shaped CuGHG single crystal with size up to around 2 mm in length (Figure 2d). Remarkably, when observed between crossed polars, the entire crystal becomes dark (extinct) simultaneously at four orthogonal positions upon a complete rotation of the microscope stage, as expected for an optically anisotropic single crystal.[41] Figure 2d shows, for example, three different orientations of the crystals with respect to the crossed polars with the first complete extinction occurring for a rotation of 40° from the initial position (see also Supplementary Video 5). This observation confirms that the comb-shaped crystal obtained is indeed a single crystal with the same lattice orientation in the main stick and the teeth and no twinning.[42] In addition, interference colors are clearly observed, changing from blue through orange/red to yellow at the border of the crystals (Figure 2d). This change corresponds to a decrease in crystal thickness according to Michael−Levy birefringence chart[41] and reflects the shape of the microchannel cross-section (Supplementary Figure 6). In addition to branched and comb-shaped CuGHG crystals, we could also prove the formation of nonequilibrium 2D morphologies featuring extended planar surfaces, i.e., millimeter-sized crystals with a height of 200 μm and width-to-height ratios up to 9:1 (Figure 2e and Supplementary Figure 12). To this aim, we exploited confinement along the vertical direction, *Z*, achieved within a high-aspect ratio device (Type III device) (Supplementary Figure 12). Both Figure 2e and Supplementary Video 6 show that as soon as the growing crystal touches the ceiling of the chamber (yellow dashed line in Figure 2e(i)), growth continues only along the *X* and *Y* (in-plane) directions, yielding CuGHG single crystals with planar morphologies (see also Supplementary Figure 12).

In order to achieve further control over the size and shape of CuGHG single crystals, we investigated their growth in Type II devices but now with a continuous feeding of the precursor solution flowing through the multiple inlet channels (Figure 3a). It should be noted that a continuous feeding permits removal of the dependence of crystal growth kinetics on molecular diffusion by preventing precursor depletion.[43] Specifically, in these experiments, we exposed preformed crystals obtained via a confined growth method to a continuous flow of an equimolar solution of Cu^{2+} and GHG at different concentrations and at a flow rate of 1 μL min^{-1} (Figure 3a). Depending on the concentration of the feeding solution, continuous growth or shrinkage of the crystals was observed and recorded by time-lapse microscopy (Figure 3b and Supplementary Video 7). The area vs time plots indicate a broadly linear trend (Figure 3c), indicating a uniform growth/dissolution rate. This is in contrast to the sigmoidal behavior observed for static growth in confined spaces (Figure 1c and 1e). This indicates that CuGHG crystals continue to grow as long as the flow of precursor solution is maintained or if the physical boundaries of the channels do not restrain growth. In fact, under conditions of constant feeding, monomer depletion does not occur and the concentration around the crystal is maintained at a supercritical level, ensuring that growth is not limited by molecular diffusion.[43] On the other hand, at subcritical concentrations, dissolved material is consistently removed from the crystal's surroundings, leading to continuous shrinkage until crystal dissolution is complete. By plotting the growth rates obtained from linear fitting at various concentrations, we could clearly identify a shrinking and a growing region delineated by a critical concentration (C_c) of approximately 100 mM (Figure 3d). At the critical concentration, crystal size does not change appreciably with time while the precursor solution flows, meaning that the growth rate equals the dissolution rate. Finally, we note that crystal growth is faster under continuous feeding conditions than under confined growth at the same precursor concentration (when above C_c). As a comparison, we exposed two preformed crystals of comparable size (approximately 38 000 μm^2) to a 200 mM precursor solution under either continuous flow (1 μL min^{-1}) or static conditions. In the former case, continuous growth at a constant rate of 27 μm^2 s^{-1} was observed (Figure 3c, red line) with the crystal area nearly tripling over 40 min (compare i and iii in Figure 3b). In the latter case the crystal displayed nonlinear growth, with a size plateau only 5% bigger than the starting value reached in about 1 h, corresponding to an average speed of 0.5 μm^2 s^{-1} (Supplementary Figure 13). To conclude, these results demonstrate that a constant supply of precursors under continuous flow conditions can be an efficient tool for controlling the growth of peptide-based MOF single crystals on the mesoscale. To the best of our knowledge, this is the first example of continuous out-of-equilibrium fed-growth of a MOF single crystal.

Finally, we show how the advection-free conditions in our microgravity-mimicking environments enabled an unexpected regrowth of CuGHG single crystals in response to laser-induced damage (Figure 3e). In these experiments, limited mass transfer—in the absence of a constant feeding or removal of precursors—enabled generation of a high local monomer concentration, which is available for fast and complete healing. Specifically, when CuGHG single crystals obtained by confined growth were irradiated with green laser light (523 nm, 10−20 s), major crystal damage was observed in the form of a local destruction or dissolution of the crystal in the irradiated portion (Figure 3e: panels i and ii). Impressively, damage of the crystal close to an edge that is in contact with the solution can be repaired through complete regrowth, as soon as irradiation is terminated, with full recovery of the original shape (iii in Figure 3e and Supplementary Video 8). Regrowth of the damaged zone is extremely fast when compared to the average growth speed observed in static confined growth experiments, lasting a few minutes (11 min in the example of Figure 3e). Remarkably, no appreciable growth along other crystal directions was observed during the healing of the damaged part. Furthermore, the destruction/regrowth sequence could be repeated several times (up to six times in the case of the crystal shown in Figure 3e) with no variations in observed behavior (Supplementary Video 8). We suggest that exposure to 532 nm laser irradiation leads to electronic excitation of metal−ligand moieties, with absorbed energy being converted into heat. Such localized heating promotes depolymerization, probably yielding monomeric CuGHG(aq) complex, which results in crystal dissolution. This mechanism is analogous to that reported for other metallosupramolecular polymers, which undergo decomplexation upon UV irradiation.[44] Accordingly, the formed concentration gradient is not easily dissipated through the surrounding media, as it would occur in bulk conditions, allowing for perfect regrowth. Importantly, the few reported examples of self-healing of

https://dx.doi.org/10.1021/jacs.0c01935
J. Am. Chem. Soc. 2020, 142, 9372−9381

crystalline materials concern molecular or macromolecular crystals that are capable of self-healing in response to small physical defects such as cracks or cuts.[45,46] Such behavior relies on the presence of reversible and dynamic bonding interactions within or between the constituents of the lattice.[46] Conversely, herein. we show that CuGHG single crystals can undergo regrowth in response to extensive induced damage of the irradiated area with recovery of the original shape.

CONCLUSION

Herein, we leveraged the special physicochemical conditions offered by microfluidic environments to obtain peptide-based MOF single crystals with complex nonequilibrium shapes and sizes up to the millimeter scale. In particular, precise control of local concentration gradients enabled by advection-free environments and the presence of confined spaces mimic two main strategies of morphogenesis in biomineralization. In addition, we studied the growth kinetics and the evolution of crystal morphology at the single-crystal level with data being analyzed in the framework of reaction−diffusion theory. This provided a unique insight into the mechanisms underlining the development of complex morphologies, i.e., local concentration gradients, physical constraints, and surface growth kinetics. Furthermore, the continuous feeding of precursors under continuous flow offers an additional efficient level of regulation over the size and shape of MOF single crystals. It should be noted that our biomimetic approach, generating monolith single crystals, also enables an efficient packing of soft porous networks inside microfluidic channels. Significantly, this result overcomes problems associated with palletization and densification of these materials for their successful implementation in functional devices.[47] We are confident that the results presented herein combined with the potential of this family of chiral solids for enantioselective separation of drugs[23,24] will open the door for development of advanced chiral stationary phases for high-throughput HPLC separations of relevance to the pharmaceutical industry. We believe that by mastering the principles presented here, increasingly complex morphologies for single crystals of soft porous frameworks can be attained while tailoring their shape- and size-specific applications. This last aspect is likely to expand further the field of application and the future of this novel class of materials.

EXPERIMENTAL SECTION

Materials and Reagents. The tripeptides H-Gly-L-His-Gly-OH and H-Gly-L-His-L-Lys-OH were purchased from BACHEM. Copper(II) acetate monohydrate was purchased from Sigma-Aldrich. All reagents were used without additional purification. Freshly prepared Milli-Q water was used to prepare all of the solutions.

Microfluidic PDMS-Based Devices. Type I and Type II double-layer microfluidic devices were prepared in polydimethylsiloxane (PDMS) by standard replica molding (see Supplementary Note 1 for further details).[48] Type I microfluidic devices comprise a branched fluid layer connected to four inlets and a control layer including three sets of pneumatic valves connected to N_2 inlets. Actuation of the pneumatic valves allowed the isolation of 11−20 elongated microchambers with volumes ranging between 0.6 and 6.4 nL (further details in Supplementary Figure 1). Type II devices were comprised of a branched fluid layer connected to 9 inlets and a bottom control layer including 11 pneumatic valves. By proper actuation of the different valves the device can be used either for confined growth experiments or for continuous feeding experiments (further details in Supplementary Figure 2). Type III devices are square single-layer PDMS devices fabricated using a square master mold and then assembled on a PDMS spin-coated glass slide by oxygen plasma bonding (Supplementary Figure 12).

Confined Growth of CuGHG Crystals in Type I Microfluidic Devices and Time-Course Visualization. In a typical experiment, a proper amount of solid glycyl-L-histidylglycine (GHG) peptide was dissolved in an equimolar solution of copper(II) acetate in a 1 mL Eppendorf tube to have a 1:1 Cu/GHG solution between 100 and 250 mM. Shaking and brief vortexing (<5 s) resulted in a completely homogeneous deep-blue solution that was immediately injected into a Type I microfluidic device, and inlets were stoppered. We note that concentrations above 250 mM were found to yield nucleation off-chip, i.e., prior to injection, while concentrations below 100 mM were subject to a long lag phase (>3 h) or absence of nucleation. In addition, vortexing time appeared to affect the rate and extent of nucleation, with overlong vortexing yielding prompt and increased nucleation. Consequently, vortexing was limited to a maximum of 5 s, which allowed us to successfully load the Type I devices without prior off-chip nucleation. Afterward, actuation of pneumatic valves allowed us to isolate various crystallization microchambers. After variable lag times, deep blue polyhedral CuGHG crystals started to appear (nucleate), and their growth was recorded using a color Retiga R1 CCD camera mounted on Nikon Eclipse T*i*-U inverted microscope with 4× or 20× Plain Fluor objectives. In the ideal scenario, 1−2 crystals formed in a single chamber, allowing for direct visualization and assessment of the growth kinetics. Time-lapse optical imaging using Ocular Image Analysis Software allowed us to record the appearance and growth of single crystals with time.

Image Analysis. Preprocessing of images (merging of RGB channels, concatenation of stacks, cropping) was carried out using ImageJ. Probability maps were generated using an image segmentation algorithm: the Weka Trainable Segmentation plugin of ImageJ, which is a machine-learning tool for pixel classification.[37] To achieve accurate segmentation, a previously trained base classifier was trained briefly upon the image in question. We note that the similarities in pixel color and intensity of microchannel walls and CuGHG MOF crystals prevented the use of normal thresholding tools. However, Weka Trainable Segmentation provided an efficient method to produce binary probability maps that were then subject to thresholding using ImageJ. Finally, the Analyze Particles function of ImageJ was used to determine the crystal area and perimeter over the frames of the time-lapse recordings. The effective perimeter P_{eff} used in the numerical model (see below) was calculated by subtracting from the total crystal outline the portion of the crystal in contact with the channel walls as determined by image analysis.

Determination of the Diffusion Coefficient of CuGHG Complex by ^{1}H DOSY NMR. Five millimolar solutions of equimolar Cu^{2+} and GHG peptide in D_2O for DOSY NMR experiments were prepared by dissolving 4 mg of solid glycyl-L-histidylglycine (GHG) peptide in 2.970 mL of a 5 mM copper(II) acetate solution in D_2O (see further discussion in Supplementary Note 4). The spectra were recorded using a Bruker 500 NMR Avance III NMR spectrometer with a resonating frequency for ^{1}H of 500.26 MHz. Measurements were performed at 298 K, and no spinning was applied to the NMR tube. The diffusion experiments were performed using a double-stimulated echo-pulse sequence for suppression of convection artifacts. The pulsed gradient was varied linearly in 16 steps.

Solubility Measurements. Equilibrium solubility of CuGHG was determined by bulk crystallization studies. Previously, a standard curve for absorbance (at 601 nm) versus concentration of 1:1 Cu/GHG solutions in the range 20−160 mM was built using an Agilent Cary 60 UV−vis spectrophotometer (Supplementary Note 4 and Supplementary Figure 8). Subsequently, 150 mM 1:1 Cu/GHG solutions (400 μL) were prepared in triplicate in 1 mL Eppendorf tubes and shaken in a thermoshaker at 24 °C, inducing crystallization. The solutions were kept in the thermoshaker until the supernatant concentration was determined to be constant (72−96 h). From the absorbance of the supernatant solution and using the built standard curve, the equilibrium solubility (saturation) of the chelate CuGHG-(aq) complex in water was determined.

https://dx.doi.org/10.1021/jacs.0c01935
J. Am. Chem. Soc. 2020, 142, 9372−9381

Growth of CuGHG Crystals under Continuous Feeding in Type II Devices. Previously, CuGHG crystals were grown under confined growth in a Type II device with a main channel of 300 μm (Supplementary Figure 2). Once the crystals had reached an appropriate size, a fresh solution of precursors was continuously injected into the main channel via a World Precision Instruments AL1000-220 syringe pump system at a flow rate of 1 μL min^{-1} and at various concentrations between 50 and 300 mM while keeping the lateral branches of the fluid layer closed by actuation of the respective pneumatic valves. At this flow rate, no appreciable drift of the crystals was observed. Depending on the concentration of the feeding solution, continuous growth or shrinkage of the crystals was observed and recorded for a period of 1−2 h by time-lapse microscopy. In each case, an upstream CuGHG crystal was selected for image analysis and the crystal area was calculated using ImageJ as described above. Area versus time plots were fitted using linear regression. The rate of growth/dissolution at different concentrations was calculated from the slope of the linear fitting.

Laser-Induced Blasting and Regrowth of CuGHG Crystals. CuGHG crystals previously prepared under confined growth, and thus surrounded by a depleted solution of precursors, were irradiated with a 532 nm green laser focused onto the crystal by a 40× Nikon objective equipping a Horiba XploRA INV Raman Microscope. Typically 10−20 s of irradiation resulted in a localized damage of the crystal with a clear blasting of the region irradiated. Immediately after stopping the irradiation, complete regrowth of the damaged crystal area was observed to occur within a few minutes, which was recorded by time-lapse imaging using a iDS UI-3070CP color camera (Supplementary Video 8).

Crystal Growth Model. We set a physical model in the framework of reaction-diffusion (RD) theory for simulating the changes of the crystal area as a function of time and fitting the experimental data. The full derivation of the model and the explanation of numerical approach are reported in Supplementary Note 2.

We consider that the increase in area $A(t)$ is proportional to the actual perimeter of the crystal in contact with solution, defined as the effective perimeter, P_{eff}, and to supersaturation $(C_t(t) - C^*)$ through the global kinetic constant k_G

$$\frac{dA(t)}{dt} = k_G P_{eff}(C_t(t) - C^*) \tag{1}$$

where $C_t(t)$ is the average concentration of the precursor solution at a certain time t and C^* is the average concentration of the depleted precursor solution surrounding a fully grown crystal (i.e., when the crystal stops growing).

Since crystal growth occurs within closed chambers of known geometry (cross section, A_s, length, l, and volume, V_0) and because we know the initial concentration of precursors, C_0, the molar mass MW of CuGHG, and the density of the crystalline porous phase of CuGHG, ρ_c, the latter determined by X-ray diffraction measurements, we can write a mass balance equation (in number of moles) as

$$C_0 V_0 = C_t(t) V_0 + \rho_c \frac{V_c(t)}{MW} \tag{2}$$

where $V_c(t)$ is the volume of the crystal that we can correlate to the measured $A(t)$ through

$$V_c(t) = A(t)h \tag{3}$$

where h is the average height of the crystal approximated to the height of a rectangle having the same area as the channel cross section (Supplementary Figure S6). Because of the channel aspect ratio, the growing crystals tend to fill quickly the channel height—the shortest dimension—and continue to grow nearly two dimensionally. From eqs 2 and 3, after rearranging we can express $C_t(t)$ as a function of the initial concentration, C_0, and of the mass (number of moles) incorporated in the crystal at time t

$$C_t(t) = C_0 - \rho_c \frac{A(t)h}{MW \cdot V_0} \tag{4}$$

We define ρ^* [mol μm^{-5}], including geometrical and material properties, as

$$\rho^* = \frac{\rho_c h}{MW \cdot V_0} \tag{5}$$

Combining eqs 1, 4, and 5 and expressing C^* as a fraction of the initial concentration ($C^* = \sigma_{eff} C_0$) we obtain a first-order nonlinear ordinary differential equation (ODE) in $A(t)$

$$\frac{dA(t)}{dt} = k_G P_{eff}((1 - \sigma_{eff})C_0 - \rho^* A(t)) \tag{6}$$

where $1 - \sigma_{eff}$ can be considered as an effective yield of crystallization representing the actual fraction of the starting materials incorporated in the crystal at the plateau.

According to RD theory, crystal growth can be represented by two consecutive coupled steps, namely, diffusion of solute from the bulk solution to the crystal−solution interface and its integration into the growing crystal (surface reaction). The two processes occur in series and offer a different resistance to crystal growth.[34] In the framework of the "two resistances in series model" (Supplementary Note 2), the experimental growth rate constant can be expressed as

$$k'_G = \frac{k'_d k'_r}{k'_r(1 - w_b) + k'_d} \tag{7}$$

where k'_d and k'_r represent the mass transfer coefficients (rate constants) for diffusion and integration, respectively, and w_b is the solution concentration expressed as mass fraction.[34] We can use eq 7 to express the overall growth rate in eq 6 through $k_G = k'_G \cdot MW \cdot \rho_C^{-1}$ (Supplementary Note 2). Thus, the method allows us to evaluate the relative contribution of these two processes to the crystal growth rate and find the rate-determining step.

Equation 6 has been used to fit numerically the experimental crystal area versus time profiles. In the fitting procedure, the solver is fed with the experimental values of $A(t)$ and $P_{eff}(t)$ obtained by image analysis, interpolating the latter at each iteration over the time step of the solver, and a minimization problem is run. First, we built a function in MATLAB whose output is the distance (summed square of residuals) between the experimental $A(t)$ profiles and those calculated by numerical integration for initial guesses of k_d, k_r, and σ_{eff} and a given set of boundary conditions (the same as in the experiments). Afterward, we calculated its global minimum using the Global Search option (with fmincon solver) within the MATLAB Global Optimization Toolbox, giving the best value for fitting parameters (i.e., k_d, k_r, and σ_{eff}). We note that k_G, represented in our growth model is a function of time (i.e., $k_G(t)$), and its values decrease with time as crystallization proceeds.

■ ASSOCIATED CONTENT

Supporting Information

The Supporting Information is available free of charge at https://pubs.acs.org/doi/10.1021/jacs.0c01935.

Microfluidic chip design and fabrication; nucleation and growth of CuGHG crystals in elongated microchambers; X-ray diffraction analysis of CuGHG crystals produced by confined growth in a Type I microfluidic device; extracting the kinetics of CuGHG crystallization from the confined growth experiments; kinetic model of crystal growth in the framework of reaction−diffusion (RD) theory; results from the numerical fitting; investigation of CuGHG(aq) chelate complex in solution by UV−vis and ^{1}H DOSY-NMR; further growth of CuGHG crystals fed under static conditions (PDF)

https://dx.doi.org/10.1021/jacs.0c01935
J. Am. Chem. Soc. 2020, 142, 9372−9381

Nucleation and confined growth of CuGHG crystals in a Type I device (MP4)

Example of image segmentation and particles analysis to extract crystal growth kinetics (MP4)

Confined growth of a CuGHG crystal taking the shape of a linear microchamber (MP4)

Confined growth of a branched CuGHG crystal within a Type II device (MP4)

Rotating a comb-shaped CuGHG crystal between crossed polars (MP4)

Shaping a CuGHG crystal into a 2D flat morphology (MP4)

Crystal growth/shrinking under continuous feeding (MP4)

Crystal regrowth after laser induced blasting (MP4)

AUTHOR INFORMATION

Corresponding Authors

Carlos Martí-Gastaldo − *Instituto de Ciencia Molecular (ICMol), Universidad de Valencia, 46980 Paterna, Spain;* orcid.org/0000-0003-3203-0047; Email: carlos.marti@uv.es

Josep Puigmartí-Luis − *Institute of Chemical and Bioengineering, Department of Chemistry and Applied Biosciences, ETH Zurich, Zurich 8093, Switzerland;* orcid.org/0000-0002-7510-9815; Email: josep.puigmarti@chem.ethz.ch

Authors

Alessandro Sorrenti − *Institute of Chemical and Bioengineering, Department of Chemistry and Applied Biosciences, ETH Zurich, Zurich 8093, Switzerland*

Lewis Jones − *Institute of Chemical and Bioengineering, Department of Chemistry and Applied Biosciences, ETH Zurich, Zurich 8093, Switzerland*

Semih Sevim − *Institute of Chemical and Bioengineering, Department of Chemistry and Applied Biosciences, ETH Zurich, Zurich 8093, Switzerland*

Xiaobao Cao − *Institute of Chemical and Bioengineering, Department of Chemistry and Applied Biosciences, ETH Zurich, Zurich 8093, Switzerland;* orcid.org/0000-0003-2211-2823

Andrew J. deMello − *Institute of Chemical and Bioengineering, Department of Chemistry and Applied Biosciences, ETH Zurich, Zurich 8093, Switzerland;* orcid.org/0000-0003-1943-1356

Complete contact information is available at: https://pubs.acs.org/10.1021/jacs.0c01935

Notes

The authors declare no competing financial interest.

ACKNOWLEDGMENTS

This work was partially supported by the European Union (ERC-2015-STG microCrysFact 677020 and ERC Stg Chem-fs-MOF 714122), the Swiss National Science Foundation (Project nos. 200021_160174 and 200021 181988), and the Spanish MINECO (MDM-2015-0538 and CTQ2017-83486-P).

REFERENCES

(1) Mann, S. *Biomineralization: Principles and Concepts in Bioinorganic Materials Chemistry*; Oxford University Press, 2001.

(2) Mann, S. Molecular Tectonics in Biomineralization and Biomimetic Materials Chemistry. *Nature* **1993**, *365* (6446), 499−505.

(3) Addadi, L.; Weiner, S. Control and Design Principles in Biological Mineralization. *Angew. Chem., Int. Ed. Engl.* **1992**, *31* (2), 153−169.

(4) Addadi, L.; Gal, A.; Faivre, D.; Scheffel, A.; Weiner, S. Control of Biogenic Nanocrystal Formation in Biomineralization. *Isr. J. Chem.* **2016**, *56* (4), 227−241.

(5) Nudelman, F.; Sommerdijk, N. A. J. M. Biomineralization as an Inspiration for Materials Chemistry. *Angew. Chem., Int. Ed.* **2012**, *51* (27), 6582−6596.

(6) Sigel, A.; Sigel, H.; Sigel, R. K. O. *Biomineralization: From Nature to Application*; John Wiley & Sons, 2008.

(7) Park, R. J.; Meldrum, F. C. Synthesis of Single Crystals of Calcite with Complex Morphologies. *Adv. Mater.* **2002**, *14* (16), 1167−1169.

(8) Li, H.; Xin, H. L.; Muller, D. A.; Estroff, L. A. Visualizing the 3D Internal Structure of Calcite Single Crystals Grown in Agarose Hydrogels. *Science* **2009**, *326* (5957), 1244−1247.

(9) Sommerdijk, N. A. J. M.; van Leeuwen, E. N. M.; Vos, M. R. J.; Jansen, J. A. Calcium Carbonate Thin Films as Biomaterial Coatings Using DNA as Crystallization Inhibitor. *CrystEngComm* **2007**, *9* (12), 1209−1214.

(10) Stock, N.; Biswas, S. Synthesis of Metal-Organic Frameworks (MOFs): Routes to Various MOF Topologies, Morphologies, and Composites. *Chem. Rev.* **2012**, *112* (2), 933−969.

(11) Seoane, B.; Castellanos, S.; Dikhtiarenko, A.; Kapteijn, F.; Gascon, J. Multi-Scale Crystal Engineering of Metal Organic Frameworks. *Coord. Chem. Rev.* **2016**, *307*, 147−187.

(12) Furukawa, S.; Reboul, J.; Diring, S.; Sumida, K.; Kitagawa, S. Structuring of Metal−Organic Frameworks at the Mesoscopic/Macroscopic Scale. *Chem. Soc. Rev.* **2014**, *43* (16), 5700−5734.

(13) Shen, K.; Zhang, L.; Chen, X.; Liu, L.; Zhang, D.; Han, Y.; Chen, J.; Long, J.; Luque, R.; Li, Y.; Chen, B. Ordered Macro-Microporous Metal-Organic Framework Single Crystals. *Science* **2018**, *359* (6372), 206−210.

(14) Hong, H.; Liu, J.; Huang, H.; Atangana Etogo, C.; Yang, X.; Guan, B.; Zhang, L. Ordered Macro−Microporous Metal−Organic Framework Single Crystals and Their Derivatives for Rechargeable Aluminum-Ion Batteries. *J. Am. Chem. Soc.* **2019**, *141* (37), 14764−14771.

(15) Ramachandran, G. N.; Sasisekharan, V. Conformation of Polypeptides and Proteins. In *Advances in Protein Chemistry*; Anfinsen, C. B., Anson, M. L., Edsall, J. T., Richards, F. M., Eds.; Academic Press, 1968; Vol. 23, pp 283−437.

(16) Beck, D. A. C.; Alonso, D. O. V.; Inoyama, D.; Daggett, V. The Intrinsic Conformational Propensities of the 20 Naturally Occurring Amino Acids and Reflection of These Propensities in Proteins. *Proc. Natl. Acad. Sci. U. S. A.* **2008**, *105* (34), 12259−12264.

(17) del Sol, A.; Tsai, C.-J.; Ma, B.; Nussinov, R. The Origin of Allosteric Functional Modulation: Multiple Pre-Existing Pathways. *Structure* **2009**, *17* (8), 1042−1050.

(18) Rabone, J.; Yue, Y.-F.; Chong, S. Y.; Stylianou, K. C.; Bacsa, J.; Bradshaw, D.; Darling, G. R.; Berry, N. G.; Khimyak, Y. Z.; Ganin, A. Y.; et al. An Adaptable Peptide-Based Porous Material. *Science* **2010**, *329* (5995), 1053−1057.

(19) Katsoulidis, A. P.; Antypov, D.; Whitehead, G. F. S.; Carrington, E. J.; Adams, D. J.; Berry, N. G.; Darling, G. R.; Dyer, M. S.; Rosseinsky, M. J. Chemical Control of Structure and Guest Uptake by a Conformationally Mobile Porous Material. *Nature* **2019**, *565* (7738), 213.

(20) Martí-Gastaldo, C.; Antypov, D.; Warren, J. E.; Briggs, M. E.; Chater, P. A.; Wiper, P. V.; Miller, G. J.; Khimyak, Y. Z.; Darling, G. R.; Berry, N. G.; Rosseinsky, M. J. Side-Chain Control of Porosity Closure in Single- and Multiple-Peptide-Based Porous Materials by Cooperative Folding. *Nat. Chem.* **2014**, *6* (4), 343−351.

(21) Katsoulidis, A. P.; Park, K. S.; Antypov, D.; Martí-Gastaldo, C.; Miller, G. J.; Warren, J. E.; Robertson, C. M.; Blanc, F.; Darling, G. R.; Berry, N. G.; et al. Guest-Adaptable and Water-Stable Peptide-Based Porous Materials by Imidazolate Side Chain Control. *Angew. Chem., Int. Ed.* **2014**, *53* (1), 193−198.
(22) Martí-Gastaldo, C.; Warren, J. E.; Briggs, M. E.; Armstrong, J. A.; Thomas, K. M.; Rosseinsky, M. J. Sponge-Like Behaviour in Isoreticular Cu(Gly-His-X) Peptide-Based Porous Materials. *Chem. - Eur. J.* **2015**, *21* (45), 16027−16034.
(23) Corella-Ochoa, M. N.; Tapia, J. B.; Rubin, H. N.; Lillo, V.; González-Cobos, J.; Núñez-Rico, J. L.; Balestra, S. R. G.; Almora-Barrios, N.; Lledós, M.; Güell-Bara, A.; Cabezas-Giménez, J.; Escudero-Adán, E. C.; Vidal-Ferran, A.; Calero, S.; Reynolds, M.; Martí-Gastaldo, C.; Galán-Mascarós, J. R. Homochiral Metal−Organic Frameworks for Enantioselective Separations in Liquid Chromatography. *J. Am. Chem. Soc.* **2019**, *141* (36), 14306−14316.
(24) Navarro-Sánchez, J.; Argente-García, A. I.; Moliner-Martínez, Y.; Roca-Sanjuán, D.; Antypov, D.; Campíns-Falcó, P.; Rosseinsky, M. J.; Martí-Gastaldo, C. Peptide Metal−Organic Frameworks for Enantioselective Separation of Chiral Drugs. *J. Am. Chem. Soc.* **2017**, *139* (12), 4294−4297.
(25) Horike, S.; Shimomura, S.; Kitagawa, S. Soft Porous Crystals. *Nat. Chem.* **2009**, *1* (9), 695−704.
(26) Koszelak, S.; Day, J.; Leja, C.; Cudney, R.; McPherson, A. Protein and Virus Crystal Growth on International Microgravity Laboratory-2. *Biophys. J.* **1995**, *69* (1), 13−19.
(27) Bird, R. B.; Stewart, W. E.; Lightfoot, E. N. *Transport Phenomena*; John Wiley & Sons, 2006.
(28) Hansen, C.; Quake, S. R. Microfluidics in Structural Biology: Smaller, Faster··· Better. *Curr. Opin. Struct. Biol.* **2003**, *13* (5), 538−544.
(29) Hansen, C. L.; Skordalakes, E.; Berger, J. M.; Quake, S. R. A Robust and Scalable Microfluidic Metering Method That Allows Protein Crystal Growth by Free Interface Diffusion. *Proc. Natl. Acad. Sci. U. S. A.* **2002**, *99* (26), 16531−16536.
(30) deMello, A. J. Control and Detection of Chemical Reactions in Microfluidic Systems. *Nature* **2006**, *442* (7101), 394.
(31) Sevim, S.; Sorrenti, A.; Franco, C.; Furukawa, S.; Pane, S.; deMello, A. J.; Puigmarti-Luis, J. Self-Assembled Materials and Supramolecular Chemistry within Microfluidic Environments: From Common Thermodynamic States to Non-Equilibrium Structures. *Chem. Soc. Rev.* **2018**, *47* (11), 3788−3803.
(32) Unger, M. A.; Chou, H.-P.; Thorsen, T.; Scherer, A.; Quake, S. R. Monolithic Microfabricated Valves and Pumps by Multilayer Soft Lithography. *Science* **2000**, *288* (5463), 113−116.
(33) Adawy, A.; Marks, K.; de Grip, W. J.; van Enckevort, W. J. P.; Vlieg, E. The Development of the Depletion Zone during Ceiling Crystallization: Phase Shifting Interferometry and Simulation Results. *CrystEngComm* **2013**, *15* (12), 2275−2286.
(34) Garside, J.; Mersmann, A.; Nývlt, J. *Measurement of Crystal Growth and Nucleation Rates*; IChemE, 2002.
(35) de Meester, P.; Hodgson, D. J. The Crystal and Molecular Structure of Glycyl-l-Histidyl-Glycinatocopper (II) Dihemihydrate. *Acta Crystallogr., Sect. B: Struct. Crystallogr. Cryst. Chem.* **1977**, *33* (11), 3505−3510.
(36) Osterberg, R.; Sjoberg, B.; Soderquist, R.; Haaland, A.; Pilotti, A. Models of Copper-Protein Interaction: The Crystal Structure of (Glycyl-L-Histidylglycinato)-Copper (II) Sodium Perchlorate Hydrate. *Acta Chem. Scand.* **1972**, *26* (10), 4184−4185.
(37) Arganda-Carreras, I.; Kaynig, V.; Rueden, C.; Eliceiri, K. W.; Schindelin, J.; Cardona, A.; Sebastian Seung, H. Trainable Weka Segmentation: A Machine Learning Tool for Microscopy Pixel Classification. *Bioinformatics* **2017**, *33* (15), 2424−2426.
(38) Naillon, A.; Joseph, P.; Prat, M. Sodium Chloride Precipitation Reaction Coefficient from Crystallization Experiment in a Microfluidic Device. *J. Cryst. Growth* **2017**, *463*, 201−210.
(39) Aiba, H.; Yokoyama, A.; Tanaka, H. Copper(II) Complexes of Glycyl-L-Histidine, Glycyl-L-Histidylglycine, and Glycylglycyl-L-Histidine in Aqueous Solution. *Bull. Chem. Soc. Jpn.* **1974**, *47* (6), 1437−1441.
(40) Crank, J.; Crank, E. P. J. *The Mathematics of Diffusion*; Clarendon Press, 1979.
(41) Stoiber, R. E.; Morse, S. A. *Crystal Identification with the Polarizing Microscope*; Springer Science & Business Media, 2012.
(42) Addadi, L.; Aizenberg, J.; Beniash, E.; Weiner, S. On the Concept of a Single Crystal in Biomineralization. In *Crystal Engineering: From Molecules and Crystals to Materials*; Springer, 1999; pp 1−22.
(43) Arnon, Z. A.; Vitalis, A.; Levin, A.; Michaels, T. C. T.; Caflisch, A.; Knowles, T. P. J.; Adler-Abramovich, L.; Gazit, E. Dynamic Microfluidic Control of Supramolecular Peptide Self-Assembly. *Nat. Commun.* **2016**, *7*, 13190.
(44) Burnworth, M.; Tang, L.; Kumpfer, J. R.; Duncan, A. J.; Beyer, F. L.; Fiore, G. L.; Rowan, S. J.; Weder, C. Optically Healable Supramolecular Polymers. *Nature* **2011**, *472* (7343), 334−337.
(45) Chen, Z.; Wang, G.; Xu, Z.; Li, H.; Dhôtel, A.; Zeng, X. C.; Chen, B.; Saiter, J.-M.; Tan, L. Metal−Organic Frameworks Capable of Healing at Low Temperatures. *Adv. Mater.* **2013**, *25* (42), 6106−6111.
(46) Zhang, L.; Bailey, J. B.; Subramanian, R. H.; Groisman, A.; Tezcan, F. A. Hyperexpandable, Self-Healing Macromolecular Crystals with Integrated Polymer Networks. *Nature* **2018**, *557* (7703), 86−91.
(47) Han, S.; Wei, Y.; Valente, C.; Lagzi, I.; Gassensmith, J. J.; Coskun, A.; Stoddart, J. F.; Grzybowski, B. A. Chromatography in a Single Metal−Organic Framework (MOF) Crystal. *J. Am. Chem. Soc.* **2010**, *132* (46), 16358−16361.
(48) Xia, Y.; Whitesides, G. M. Soft Lithography. *Annu. Rev. Mater. Sci.* **1998**, *28* (1), 153−184.

https://dx.doi.org/10.1021/jacs.0c01935
J. Am. Chem. Soc. 2020, 142, 9372−9381